High-speed dislocations in high strain-rate deformations

Roos, A; de Hosson, J.T.M.; van der Giessen, E.

Published in:
Computational Materials Science

DOI:
10.1016/S0927-0256(00)00118-X

Publication date:
2001

ELSEVIER

Computational Materials Science 20 (2001) 19–27

COMPUTATIONAL MATERIALS SCIENCE

www.elsevier.com/locate/commatsci

High-speed dislocations in high strain-rate deformations

A. Roos [a], J.Th.M. De Hosson [a,*], E. Van der Giessen [b]

[a] *Laboratory of Applied Physics, Materials Science Center, Netherlands Institute for Metals Research, University of Groningen, Nijenborgh 4, 9747 AG Groningen, The Netherlands*

[b] *Koiter Institute, Micromechanics of Materials Group, Netherlands Institute for Metals Research, Delft University of Technology, Mekelweg 2, 2628 CD Delft, The Netherlands*

Received 17 April 2000; accepted 16 May 2000

Abstract

In this paper, shear deformation at high strain rates is modelled within the framework of discrete dislocation plasticity. The question is addressed whether dislocation accelerations may be ignored at high strain rates. Furthermore, the usage of high-velocity stress and displacement fields are studied. The simulations take place in a computational cell representing Al and Cu that is sheared at a strain rate of 10^6 s^{-1}. The computations show that the inertial effects may not be neglected. Furthermore, although the high-velocity stress and displacement fields yield significant differences locally with respect to their quasi-static counterparts, their effect on the overall stress–strain curve is negligible.

Keywords: Dislocations; Mesoscopic length scale; Accelerations; Plastic deformation; High strain rate

1. Introduction

The companion paper [1] extended the method of Discrete Dislocation Plasticity [2–5] to capture the specific processes taking place at high strain rates and provided a physical basis for the projection of obstacle properties into the computational cell. This paper tests the validity of some approximations and provides examples to show the applicability of the method to high strain-rate deformation. In assessing the results, one has to keep in mind two underpinning aspects: (1) the model is two-dimensional and (2) the results hold only in the regime where linear isotropic elasticity is valid.

The micromechanical model has many parameters. Most of these parameters boil down to a proper selection of the initial configuration. Some parameters are easily available in the literature, such as elastic constants, material densities, magnitude of the Burgers vector. Other parameters may be provided directly by microstructural observations, with the aid of Scanning Electron Microscopy (SEM) or Transmission Electron Microscopy (TEM). Parameters of this sort are total obstacle densities, initial dislocation densities and the spacing of active slip planes. Mean jump distances and obstacle statistics may be inferred from $T_{1\rho}$-spin-lattice pulse NMR- and TEM-measurements [6].

This paper models the fast shear deformation of a strip of single crystalline Al and Cu with the primary slip planes parallel to the shear direction.

* Corresponding author. Tel.: +1-31-50-363-4898; fax: +1-31-50-363-4881.

E-mail address: hossonj@phys.rug.nl (J.Th.M. De Hosson).

0927-0256/01/$ - see front matter
PII: S0927-0256(00)00118-X

Table 1
Mechanical properties of Al and Cu

Property	Al	Cu
Young's modulus E (GPa)	70	110
Poisson's ratio ν	0.33	0.35
Material density ρ (mg m^{-3})	2.70	8.92
Burgers vector b (nm)	0.286	0.256
Drag coefficient B_{TOT} at 298 K (μPa s)	40	20

Some bulk properties of Al and Cu are listed in Table 1. The microscopic parameters, such as the concentration of solutes, size of precipitates, etc. are taken from TEM-observations [7] of an Al–Li alloy. These numbers indicate the order of magnitude for use in the simulations. In Al 2.2 wt% Li (i.e. Al 8.0 at.% Li), aged at 215°C for 1 h and at 5% deformation, the coherent Al_3Li ordered precipitates (δ') had a volume fraction of 2.9%, a mean diameter of 14.4 nm and a strength of 31 MPa. The solute solubility of Li in Al is of the order of 0.1 at.% at room temperature. An indication of the obstacle strength f_c posed by forest dislocations is given in De Hosson et al. [6]. For forest dislocations in an Al 2 at.% Zn alloy: $f_c = 0.13$, with the forest dislocations acting as Friedel obstacles. The solute atoms, acting in the Mott-Nabarro regime, bend the dislocation line over an angle with $\cos(\varphi_c) = f_c = 0.043$ before breakaway. The precise manner in which these properties project into the computational cell is discussed in the companion paper.

Section 2 looks into the matter of neglecting the inertial terms in the equation of motion. Section 3 compares the high-velocity stress and strain fields and the relativistic drag-relation with the static ones and discusses the resulting stress–strain curves.

2. Velocities and accelerations

Figs. 1 and 2 compare three cases: the case of instantaneous velocity change, which is the solution for the dislocation velocity v of the drag relation

$$b\sigma_{\mathrm{PK}} - B_{\mathrm{TOT}}(v)v = 0 \tag{1}$$

(Eq. (20) of the companion paper [1], with b the magnitude of the Burgers vector, σ_{PK} the resolved shear stress felt by the dislocation and $B_{\mathrm{TOT}}(v)$ the velocity-dependent drag coefficient [8]), the case of constant acceleration $\dot{v}$, which is the solution of

$$b\sigma_{\mathrm{PK}} - B_{\mathrm{TOT}}(v)v = m_e(v)\dot{v} \tag{2}$$

(Eq. (21) of the companion paper [1], with $m_e(v)$ the "relativistic" dislocation mass [9]), and the case where the approximation of constant acceleration has been numerically integrated over extremely small time increments ($\sim 10^{-14}$ s). These particular cases are calculated for a single dislocation in an infinite medium under a fixed stress σ_{PK}. Fig. 1 displays the results for Al and Fig. 2 for Cu. In both materials, an extreme velocity change, driven by an extreme constant stress of the order of the theoretical strength of the materials ($\sim\mu/30$), has been plotted alongside a more moderate one. The values of the drag coefficients that were used to plot these graphs are the ones given in Table 1. It can be seen that the order of magnitude of the time interval needed to reach, say, 90% of its final velocity, is of the order of a few ps for the extreme velocity change, but in Cu, the moderate velocity change takes a few tens of ps. In fact, the acceleration approaches zero after 0.5 ns.

From these plots, it cannot be concluded a priori that in the simulations of Al and Cu the accelerations may be neglected, since at this point we do not know the order of magnitude of the average time increment in the actual simulations. An upper limit for the magnitude of the average time increment is obtained by noting from the Orowan equation that

$$\bar{v}_{\mathrm{DIS}} = \frac{\dot{\gamma}}{\rho_{\mathrm{M}} b} \tag{3}$$

and then the average time increment equals the time that a dislocation needs to cross the average distance l_{average} between obstacles on its slip plane. The actual time increment is smaller, because the dislocations can also meet each other, the distance between two obstacles varies considerably around the average, and the same holds for the dislocation velocities. Using the material parameters of the introduction leads to an obstacle density of the order 5×10^{15} m^{-2} (this *very* high number is primarily caused by the solute atoms), so that

$l_{\text{average}} \cong 1.5 \times 10^{-8}$ m, and with a mobile dislocation density of $\rho_M = 10^{14}$ m^{-2} at a strain rate $\dot{\gamma} = 10^6$ s^{-1}, the average time increment $\Delta t_{\text{average}} \lesssim 3 \times 10^{-10}$ s.

Another consideration is whether in the actual simulation the stresses can change at such a high rate as in Figs. 1 and 2 (i.e. instantaneously). It is conceivable that this would happen in the late stages of the annihilation process, when two dislocations of opposite sign come very close together. Neglecting accelerations would let the dislocation change velocity from below the Rayleigh velocity to above the Rayleigh velocity *instantaneously*. Then the sign of the shear stress on the slip plane reverses, and the two dislocations repel each other (recall that we use high-velocity fields in Eqs. (5)–(7) of the companion paper). In the next time increment, the velocities will change direction, again instantaneously. The dislocations will move apart, leading to a lower velocity, possibly below the Rayleigh velocity. They will attract again, etc. The point here is that although the change in sign is possible *physically*, in the simulations it may *also* happen because of a *numerical* reason (which is neglecting the accelerations for ease and speed of computation). However, depending on the time increments in the actual simulation, we do not know whether it actually happens.

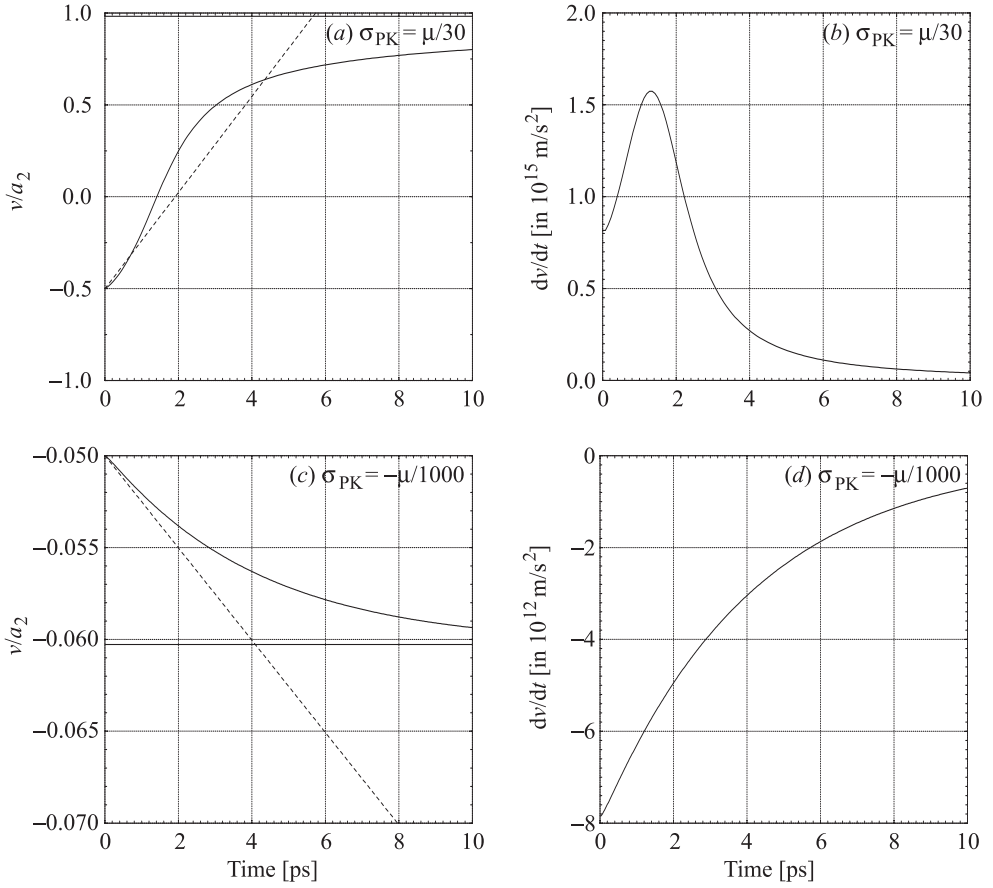

Fig. 1. Dislocation velocity v/a_2 (left) and acceleration dv/dt (right) of an edge dislocation in Al for two different cases of applied shear stress σ_{PK} and initial dislocation velocity. In the velocity plots, the dashed line denotes the approximation of constant acceleration, Eq. (2), while the horizontal lines denote the velocity when velocity changes take place instantaneously (Eq. (1). (a) and (b): $\sigma_{PK} = \mu/30$ and initial $v = -\alpha_2/2$. (c) and (d): $\sigma_{PK} = -\mu/1000$ and initial $v = -\alpha_2/20$.

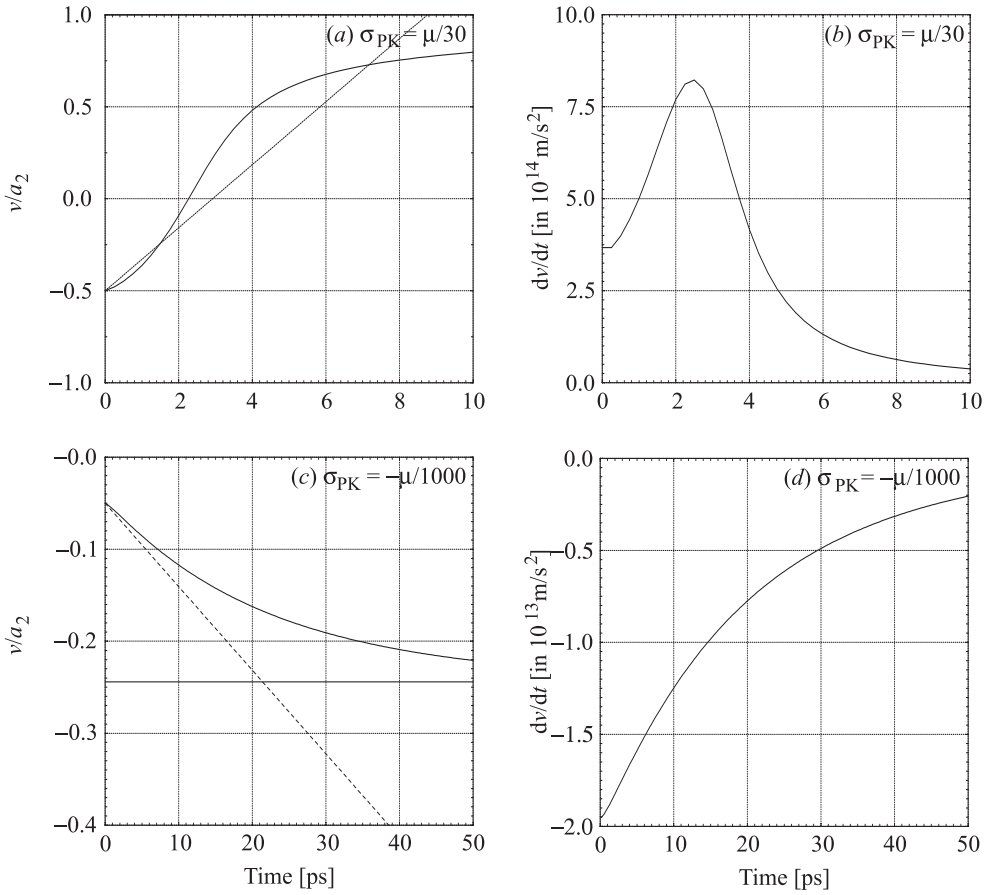

Fig. 2. As in Fig. 1, but now in Cu instead of in Al.

In order to answer this question more definitely, we will have to carry out a set of actual simulations with exactly the same parameters and initial configurations, except that one set uses the approximation of constant acceleration, and the other instantaneous velocity changes. Note that from Figs. 1 and 2, we assume that the approximation of constant acceleration is a reasonable one as long as the time increment does not exceed to the time needed to reach the final velocity. Otherwise, some cases would be possible with supersonic dislocation velocities, which is clearly in violation with linear isotropic elasticity. However, before carrying out the full simulations, we first have to ensure the numerical accuracy of other aspects of the simulations.

3. Simulations

In this section, the question will be addressed whether the high-dislocation velocities that significantly change the stress and displacement fields actually occur in the computational cell. The simulations will be carried out using material parameters representing Cu, because Cu has a low static drag coefficient: at room temperature $B^{\mathrm{Cu}}_{\mathrm{TOT}}(298\ \mathrm{K}) = 20\ \mu\mathrm{Pa\ s}$[10]. In fact, to make it even easier for the dislocations to reach the high velocities, we will take the drag coefficient $B^{\mathrm{Cu}}_{\mathrm{TOT}}(100\ \mathrm{K}) = 14\ \mu\mathrm{Pa\ s}$. This temperature is at the lower temperature limit with respect to the Debye temperature ($\theta^{\mathrm{Cu}}_{\mathrm{D}} = 343\ \mathrm{K}$) for which the temperature dependence of the static drag coefficient is linear [10].

We will also compare the cases with and without accelerations (Section 2). In the case of accelerations, the time increment is kept very small at $\Delta t = 2 \times 10^{-14}$ s. It is important to stress that this order of magnitude is for numerical reasons only. One should not attach any physical significance to this order of magnitude, since the Debye frequency is of the order of 10^{13} s^{-1}. Any events involving *collective* motion of atoms (such as dislocation motion) cannot take place at a higher rate. The calculations without accelerations use an adaptive time step. It is determined by the next *event*, where an event is a collision between two dislocations, an annihilation, generation of a dislocation loop, and pinning or release of a dislocation at an obstacle.

The computational cell has the same microstructural parameters as in the example of Al of the introduction, although with a lower volume fraction of precipitates (1%) to allow for enough room on the slip plane for the build-up of dislocation pile-ups. To stimulate this even more, the precipitates are taken a bit stronger: $f_c = 0.6$, leading to an effective obstacle strength of 50 MPa. The samples are deformed at a strain rate of 10^6 s^{-1} using a finite-element mesh of 40×40 elements in a computational cell of 2×2 μm, containing 40 slip planes. For each simulation, the total dislocation density is 10^{14} m^{-2} and the number of slip planes in 20 μm^{-1}.

A typical example of the resulting stress–strain curves is presented in Fig. 3 for 100 K. Each graph contains a curve for the case without accelerations, conventional stress and displacement fields, and a linear stress–velocity relation (lowest curve), a curve for the case with constant accelerations, conventional stress and displacement fields, and a linear stress–velocity relation, and a curve for the case with constant accelerations, relativistic stress and displacement fields, and a cubic stress–velocity relation. The latter can be derived as follows.

In our case, the main interest is in the *velocity*-dependence of B_{TOT}, especially in the high-velocity regime, which was not treated in literature extensively. Basically the overall drag coefficient B_{TOT} can be decomposed in an electronic contribution B_e and a phonon contribution B_{PH}. In the latter the thermal phonons excite vibrations in the dislocation line, which are then re-radiated in a cylindrical wave around the dislocation line. When the dislocation is moving, this gives rise to a net force opposing the motion. This is called the flutter mechanism and it is described in terms of linear elasticity [8,10,11]. The resulting drag coefficient is denoted by B_{flut}. It can be shown [8] that the static

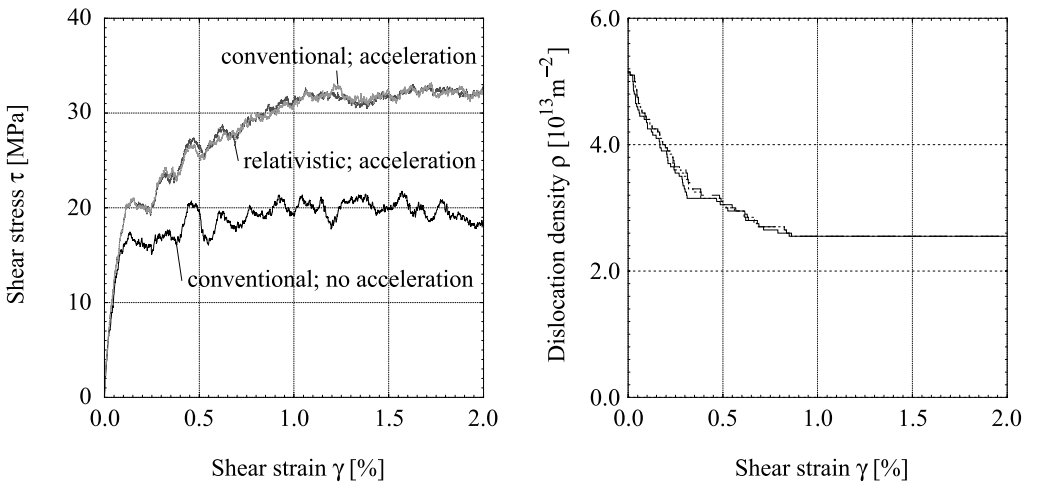

Fig. 3. Stress–strain curves in Cu at 100 K and $y = 10^6$ s^{-1} (left). The lower curve is the conventional case without acceleration; the light top curve denotes the relativistic case with acceleration and the remaining dark top curve the conventional case with acceleration. The picture to the right denotes the corresponding total dislocation densities: the solid line represents the conventional/no acceleration case, the dotted line the relativistic/acceleration case and the long-dashed line the conventional/acceleration case.

value of B_e is typically of the order of 1 μPa s or below for Cu and Al. In the limit that the dislocation velocity v_{DIS} approaches the Rayleigh v_R, these values increase at most by a factor of 1.6, so even in the high velocity-limit, the order of magnitude remains around 1 μPa s. Compared with the magnitude of the total drag coefficients in these metals, they may safely be neglected, except at very low temperatures. The velocity-dependent B_{flut} can be found by taking the Fourier transform of the velocity-dependent strain fields. This leads to [8]:

$$B_{TOT}(v_{DIS}) = B_{static} + B_{dynamic}(v_{DIS}) \approx B^0_{flut}\left(\frac{B_{static}}{B^0_{flut}} + \frac{1}{1-(v_{DIS}/a_2)^2}\right), \quad (4)$$

where the velocity-independent terms have been explicitly separated out from the velocity-dependent term. The viscous phonon drag increases as the dislocation velocity increases towards the shear wave velocity a_2. Substituting the total drag coefficient B_{TOT} into Eq. (1) gives

$$\sigma_{PK}b = B_{TOT}v_{DIS} = \left(B_{static} + \frac{B^0_{flut}}{1-v^2_{DIS}/a^2_2}\right)v_{DIS}. \quad (5)$$

The dislocation velocity in the steady state is then given by the solution of

$$\left(\frac{v_{DIS}}{a_2}\right)^3 - \frac{\sigma_{PK}b}{a_2 B_{static}}\left(\frac{v_{DIS}}{a_2}\right)^2 - \frac{B_{static}+B^0_{flut}}{B_{static}}\left(\frac{v_{DIS}}{a_2}\right) + \frac{\sigma_{PK}b}{a_2 B_{static}} = 0. \quad (6)$$

This cubic equation has three real solutions only if the coefficients fulfil certain criteria, which is the case here.

The calculations for the case without accelerations, relativistic stress and displacement fields and a the solution of (1) turned out to suffer from the numerical oscillations described at the end of Section 2 and as a result none of the calculations gave any sensible output. The histogram of the velocity distributions of the three runs is plotted in Fig. 4, where each distribution has been normalised to its maximum value.

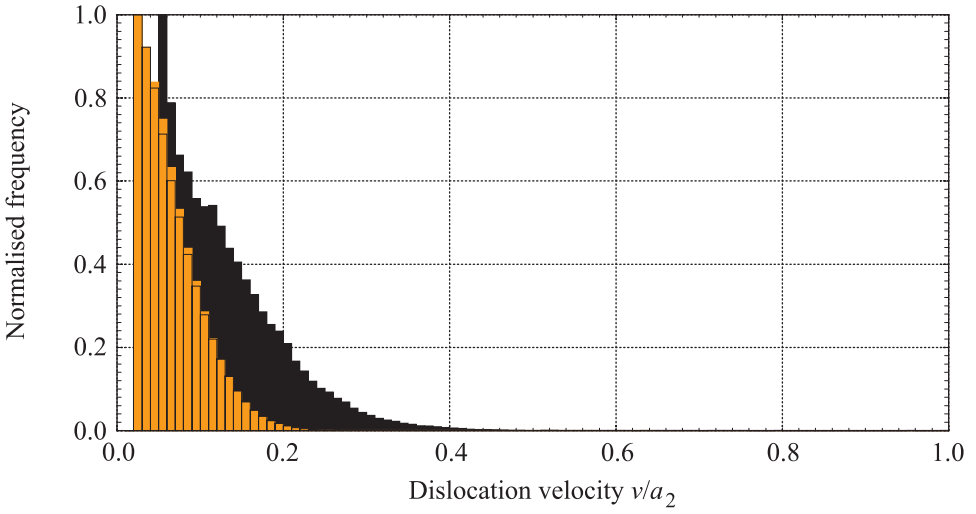

Fig. 4. Histogram of the distributions of absolute dislocation velocities of the runs of Fig. 3 at 100 K. The *black filled* histogram corresponds to the conventional case without acceleration, the *yellow filled* histogram to the relativistic case with accelerations and the *transparent outlined* histogram (which corresponds very closely to the yellow one) corresponds to the conventional case with accelerations. The histograms are obtained by repeatedly sampling the velocity-distribution after a certain number of time increments. This plot then represents the velocities during the whole simulation. The plots are normalised to their maximum value (as a result, the relative frequencies for velocities higher than about half the shear wave velocity a_2 are not visible, although generally they are not equal to zero). For the static case, the supersonic dislocations have not been counted.

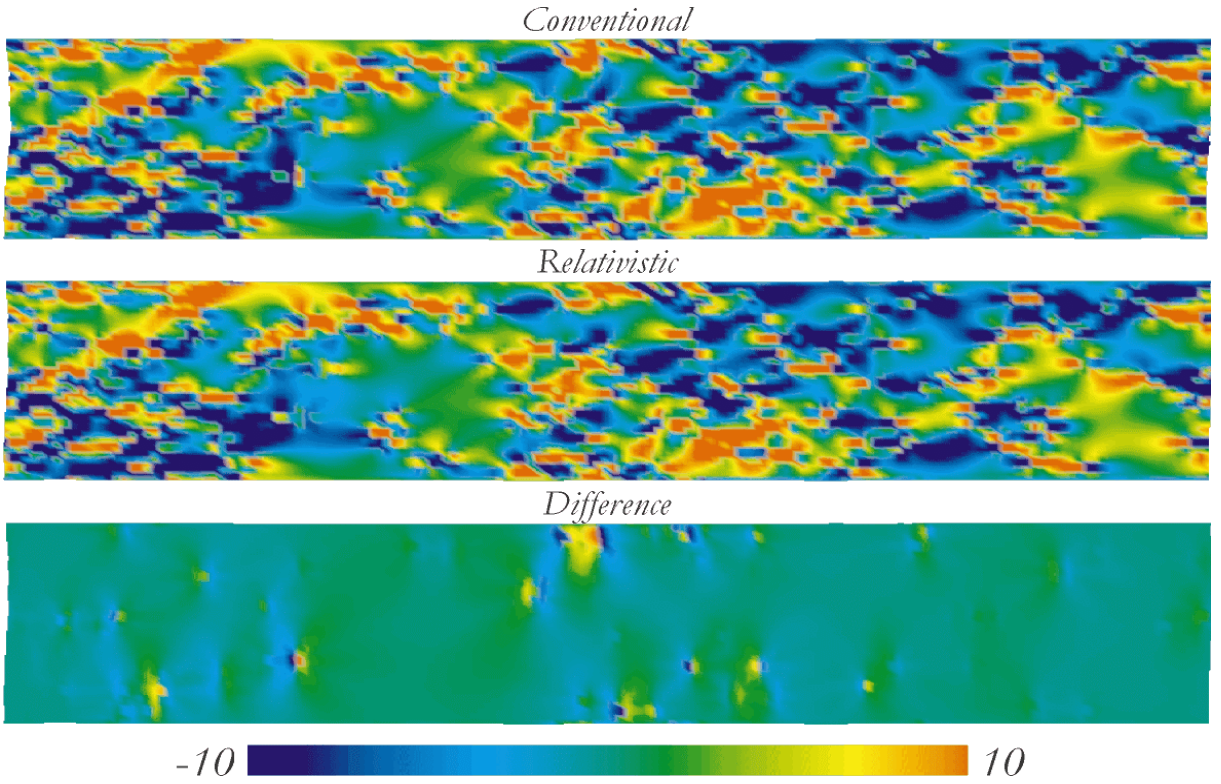

Fig. 5. Comparison of the normalised dislocation shear stress $1000\tilde{\sigma}_{12}/\mu$ between –10 and 10 of (b) relativistic and (a) conventional shear stress and (c) their difference. More comments in the text.

The effect of the changing fields on the dislocation shear stress $\tilde{\sigma}_{12}$ is depicted in Fig. 5. In this figure, taken from a different simulation than Figs. 3 and 4, the middle picture (b) represents the dislocation shear stresses in the relativistic case. Also visible (at the periodic boundaries) are the displacements. In the top picture (a) the dislocation shear stress is calculated for exactly the same configuration as picture (b), and for exactly the same dislocation velocities, but now using the conventional fields. Strictly speaking, this solution does *not* satisfy the applied boundary conditions, but the point here is to illustrate the difference in the dislocation fields. Since it is somewhat difficult to discern these differences, the two pictures have been subtracted from each other to give the difference field in the lower picture (c). The difference picture shows that locally the difference can be quite large for the few fast-moving dislocations. However, in the calculation of the overall stress and strain, the differences are smeared out over the top- and bottom-surface do not contribute significantly.

4. Discussion

The first thing that stands out in Fig. 3 is the large difference between the case without, and the cases with acceleration. In the computations with the adaptive time increment, the time increments are typically of the order of a picosecond. This is smaller than the time needed for a dislocation to settle to its steady-state velocity. In order to really make sure that the difference is not due to the adaptive time stepping (instead of a fixed time increment of 2×10^{-14} s), extra simulations (not displayed) have been carried out. The only difference is that they now *also* have a fixed time increment of 2×10^{-14} s. It turns out that the

stress–strain curve follows the curve with the adaptive time stepping almost exactly. The only difference then being the accelerations, it has to be concluded that they cannot be neglected at this high strain rate, both for the conventional and the relativistic cases.

The second point of interest is the small differences between the conventional and the relativistic case. The velocity distributions of Fig. 4 show that almost no dislocations move faster than a few tenths of the shear wave velocity. Actually, Fig. 4 shows no dislocations at all in that regime, but this is an effect of the scale. In reality, the spectrum is not zero until very close to the shear wave velocity (and beyond for the conventional case). Nevertheless, the number of dislocations that do reach the high velocities is utterly negligible with respect to the number of dislocations moving at velocities up to 20% of the shear wave velocity.

A third feature of the curves of Fig. 3 is the fact that the flow stress attains a constant value and does not show any hardening effects. The mechanisms that give rise to hardening in the computational cell are the increase in number of forest dislocations, Taylor hardening due to the interaction of the dislocations on different slip planes, and hardening due to the formation of dislocation pile-ups at obstacles. The first process is controlled by the dislocation density and is handled as described in the companion paper (Table 1, Eqs. (45)–(48)). From Fig. 3 it is seen that the dislocation density never increases. In fact, the density reached a steady-state value. The interaction between different slip planes is observed in the simulations. In simulations with a very low obstacle density, the dislocations form vertical "walls" moving collectively. The interaction is usually not strong enough to maintain these walls when one dislocation is held up by an obstacle. The last mechanism, hardening due to pile-up formation, is not observed with obstacle strengths less than about 1 GPa. This could be attained by a grain boundary, or impenetrable inclusions that are also too large to be passed by the Orowan process. Examples of those cases (yet at much lower strain rates of strain rate 10^3 s^{-1}) can be found in Van der Giessen and Cleveringa et al. [2,3] From the present work, we conclude that the hardening effects found in those cases are entirely due to the pile-ups formed against the impenetrable inclusions.

5. Conclusions

In this paper, shear deformation at high strain rates is modelled within the framework of discrete dislocation plasticity. The simulations in a two-dimensional computational cell with a microstructure representing Al and Cu show that the inertial effects may not be neglected at strain rates of the order of 10^6 s^{-1}. Furthermore, although the high-velocity stress and displacement fields yield significant differences *locally* with respect to their quasi-static counterparts, their effect on the overall stress–strain curve is negligible. Finally, it is shown that no hardening effects resulting from obstacles or forest dislocation occur at the level of stresses present in the computational cell. Rather, a steady-state stress state occurs where all dislocation activity is concentrated on a few slip planes.

Acknowledgements

The work described in this paper is supported by IOP-metals under project number C94.703.RG.TF and the Netherlands Institute for Metals Research (NIMR).

References

[1] A. Roos, J.Th.M. De Hosson, H.H.M. Cleveringa, E. Van der Giessen, Fast-moving dislocations in high strain-rate deformation, Computational Materials Science, 18 (2000).
[2] E. Van der Giessen, A. Needleman, Discrete dislocation plasticity: a simple planar model, Modelling Simul. Mater. Sci. Eng. 3 (1995) 689.
[3] H.H.M. Cleveringa, E. Van der Giessen, A. Needleman, Comparison of discrete dislocation and continuum plasticity predictions for a composite material, Acta Mater. 45 (1997) 3163.
[4] A. Roos, J.Th.M. De Hosson, H.H.M. Cleveringa, E. Van der Giessen, Shear deformation at high strain rates using fast-moving dislocations: a computer simulation methodology, in: H.J.J. Kals, M. Geiger, B. Shirvani, U.P. Singh (Eds.), Shemet 98, Twente University Press, Enschede, The Netherlands, 1998.

[5] A. Roos, J.Th.M. De Hosson, H.H.M. Cleveringa, E. Van der Giessen, A computer simulation methodology of metal perforation, in: J. Huétink, F.P.T. Baaijens (Eds.), Simulation of Materials Processing: Theory, Methods and Applications (NKumiform 98), Balkema Rotterdam, 1998, p. 303.
[6] J.Th.M. De Hosson, G. Boom, U. Schlakowski, O. Kanert, Solution hardening in Al–Zn alloys. Mean jump distance and activation length of moving dislocations, Acta Metall. 34 (1986) 1571.
[7] J.Th.M. De Hosson, A.J. Huis in't Veld, H. Tamler, O. Kanert, Dislocation dynamics in Al–Li alloys. Mean jump distance and activation length of moving dislocations, Acta Metall. 32 (1984) 1205.
[8] A. Roos, J.Th.M. Hosson, Drag forces on fast-moving dislocations, Phys. Rev. B, submitted.
[9] J.P. Hirth, H.M. Zbib, J. Lothe, Forces on high velocity dislocations, Modelling Simul. Mater. Sci. Eng. 6 (1998) 165.
[10] E. Nadgornyi, Dislocation dynamics and mechanical properties of crystals, Prog. Mater. Sci. 31 (1988).
[11] Y. Kogure, Y. Hiki, Lattice thermal conductivity of crystals containing dislocations, J. Phys. Soc. Japan 38 (1975) 471.